Dalton Transactions

Gauging Aromatic Conjugation and Charge Delocalization in the Aryl Silanes Ph_nSiH_{4-n} (n = 0-4), with Silicon K-edge XAS and TDDFT

Journal:	*Dalton Transactions*
Manuscript ID	DT-ART-09-2020-003153
Article Type:	Paper
Date Submitted by the Author:	08-Sep-2020
Complete List of Authors:	Phillips, Nicholas; University of Oxford, Chemistry Smith, Patrick; University of California Berkeley, Chemistry Tilley, T. Don; University of California, Berkeley, Chemistry Minasian, Stefan; Lawrence Berkeley National Laboratory, Chemical Sciences Division

Gauging Aromatic Conjugation and Charge Delocalization in the Aryl Silanes Ph_nSiH_{4-n} (n = 0-4), with Silicon K-edge XAS and TDDFT†

Nicholas A. Phillips,‡[a,b] Patrick W. Smith,‡[a] T. Don Tilley,*[a,b] Stefan G. Minasian*[a]

[a] Chemical Sciences Division, Lawrence Berkeley National Laboratory, Berkeley, CA 94720, United States

[b] Department of Chemistry, University of California, Berkeley CA 94720, United States

† Electronic supplementary information (ESI) available.

‡ These authors contributed equally

ABSTRACT

Si K-edge X-ray absorption spectra (XAS) have been measured experimentally and calculated using time-dependent density functional theory (TDDFT) to investigate electronic structure in aryl silanes, Ph_nSiH_{4-n} (n = 0-4). Adding aryl groups to SiH_4 splits the Si-H σ-antibonding orbitals into new orbitals with Si-Ph π-bonding (π^b) and π-antibonding (π*) character. Greater aryl substitution is reflected by increasingly intense Si 1s → π^b and Si 1s → π* transitions, and weaker transitions into the Si-H and Si-C σ* orbitals. These observations are consistent with known trends in the hydride donor ability of aryl silanes, which is driven in part by the composition of the LUMOs and the accessibility of pathways for electron delocalization through aromatic conjugation. Methodology developed for liquid-phase Si K-edge XAS measurements on $PhSiH_3$ and Ph_2SiH_2 will enable dynamic studies of chemical transformations involving silicon-containing catalysts, intermediates, and substrates.

INTRODUCTION

Aryl silanes (Ph_nSiH_{4-n}; n = 0-4) are involved in a wide range of organic transformations including as substrates in the catalytic hydrosilation of unsaturated carbon–carbon and carbon–heteroatom bonds.[1-2] During hydrosilation the Si-H bond is cleaved in either a homolytic or heterolytic fashion, often via pre-activation by a catalyst.[3-4] Catalyst systems for hydrosilation span both early and late transition metals as well as main group Lewis acids and bases. The transition metal-catalyzed hydrosilation mechanism proposed by Chalk and Harrod relies upon the oxidative addition of the Si-H bond to the transition metal center forming a reactive metal silyl complex.[5-7] Lewis acid catalysts (e.g., $B(C_6F_5)_3$) act by forming an encounter complex that polarizes the Si-H bond, facilitating attack by a Lewis basic substrate (e.g., a carbonyl).[8-9] In both cases the catalyst promotes reaction with the substrate by weakening the Si-H

interaction, either by donating electron density into Si-H σ-antibonding orbitals or by withdrawing electron density from Si-H σ-bonding orbitals.[10] Recent reports have highlighted the influence of the number of aryl substituents at silicon on both reaction mechanisms and product distributions under otherwise identical conditions.[11-12] Furthermore, hydride abstraction from a sterically unhindered diaryl(alkyl)silane generates the triarylsilylium cation, a product of redistribution at silicon.[13] Therefore, a detailed understanding of the electronic structure of how aryl substituents influence Si-H reactivity is necessary for the rational design of less expensive and more environmentally benign catalyst-silane combinations that are versatile, active, and selective. However, such detailed descriptions of electronic structure have been hard to develop for many of the most reactive systems. Much of the mechanistic understanding of hydrosilation catalysis is limited to stoichiometric transformations, particularly of diamagnetic metal complexes that can be identified by nuclear magnetic resonance (NMR) spectroscopy.[3]

Several studies have shown that X-ray absorption spectroscopy (XAS) at the K-edge for light elements is a versatile and direct probe of chemical structure and bonding in molecular inorganic systems.[14-20] The spectroscopic technique probes bound-state transitions between core 1s orbitals and unoccupied p-orbitals. Because the Si 3p orbitals are directly involved in bonding, Si K-edge XAS could be a useful tool to identify changes in Si-H, Si-C, Si-O, and Si-M bonding during hydrosilation catalysis. However, many synchrotron beamlines are not optimized in the intermediate energy regime that includes the Si K-edge (ca. 1840 eV), and uses for this technique have been limited to studies of solid oxides and minerals, and gaseous SiX_4 molecules and organosilanes.[21-29] As a result, there is little precedent for the measurement, modeling, theoretical simulation, or interpretation of Si K-edge XAS data. Herein, we combine Si K-edge XAS and density functional theory (DFT) calculations to examine the aryl silane series (Ph_nSiH_{4-n}, n = 0-4) and explore how increasing the number of aryl substituents impacts electronic structure and reactivity.

RESULTS AND DISCUSSION

Our approach utilizes a scanning transmission X-ray microscope (STXM) to mitigate saturation and self-absorption errors by detecting Si K-edge X-rays in transmission mode. Fig. 1 compares the background subtracted and normalized Si K-edge spectra obtained at room temperature for solid samples of Ph_4Si and Ph_3SiH and liquid samples of Ph_2SiH_2 and $PhSiH_3$, as well as the gas-phase spectrum for SiH_4 reported previously by Bodeur and coworkers.[22] Spectra were obtained from solid samples of using STXM raster scans according to standard methodology.[30-31] For liquid samples, a 10 μm pathlength microfluidic cell was employed (see Experimental) and photons transmitted through the cell were detected. The beam was positioned at a single point on the liquid cell and defocused to a ca. 20 μm spot size to minimize radiation damage.

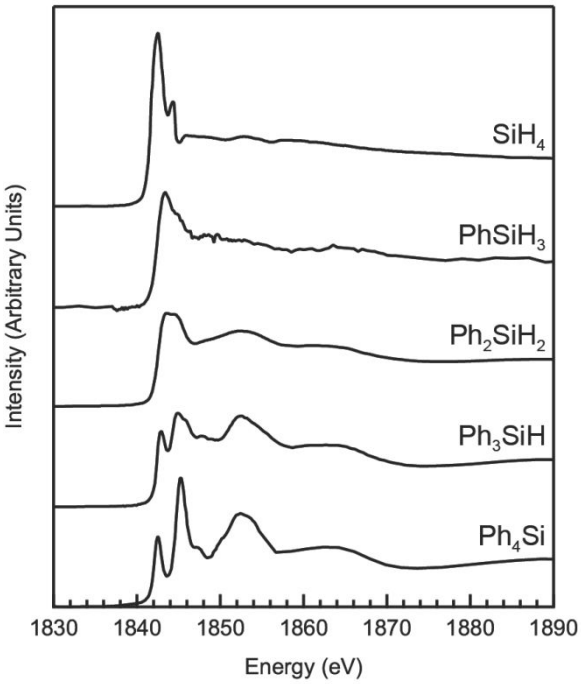

Fig. 1. Transmission Si K-edge XAS obtained at room temperature from liquid samples of $PhSiH_3$ and Ph_2SiH_2, and from solid samples of Ph_3SiH and Ph_4Si. The Si K-edge XAS data for SiH_4 was adapted with permission from S. Bodeur, P. Millie, and I. Nenner, "Single- and multiple-electron effects in the Si 1*s* photoabsorption spectra of SiX_4 (X = H, D, F, Cl, Br, CH_3, C_2H_5, OCH_3, OC_2H_5) molecules: experiment and theory," *Phys. Rev. A* **1990**, *41*, 252-263. Copyright 1990 by the American Physical Society.

Curve fits of the Si K-edge spectra are shown in Fig. 2 and summarized in Table 1 .[32] Pre-edge features were modeled using symmetrically constrained pseudo-Voigt functions and a step function. High-quality fits were obtained in each case as shown by good correlation coefficients, residual data that slightly deviated from zero, and symmetric residual peaks that were similar in shape to the corresponding pseudo-Voigt functions. In each case, care was taken to minimize the number of fitting parameters and maintain consistency in modeling the edge region. For SiH_4, $PhSiH_3$, and Ph_4Si, the first and second derivatives of the data suggested that the pre-edge regions are best modeled by two pseudo-Voigt functions. For Ph_2SiH_2 and Ph_3SiH, which have lower symmetries, three pseudo-Voigt functions are required. In some cases the spectral profiles are characterized by shoulders and few well-resolved peaks, indicating that the Si K-edge transitions are closely spaced. Because multiple curve fitting models provide good approximations of the experimental data, this introduces greater uncertainty in the parameters of their corresponding curve fit functions. However, because the uncertainties for adjacent functions are correlated, confidence increases when curve fit functions were evaluated as a group rather than individually. Consequently, average energies and total intensities are discussed for the two low energy functions in the Si K-edge XAS of Ph_2SiH_2, and for the two higher energy functions in the Si K-edge XAS of Ph_3SiH.

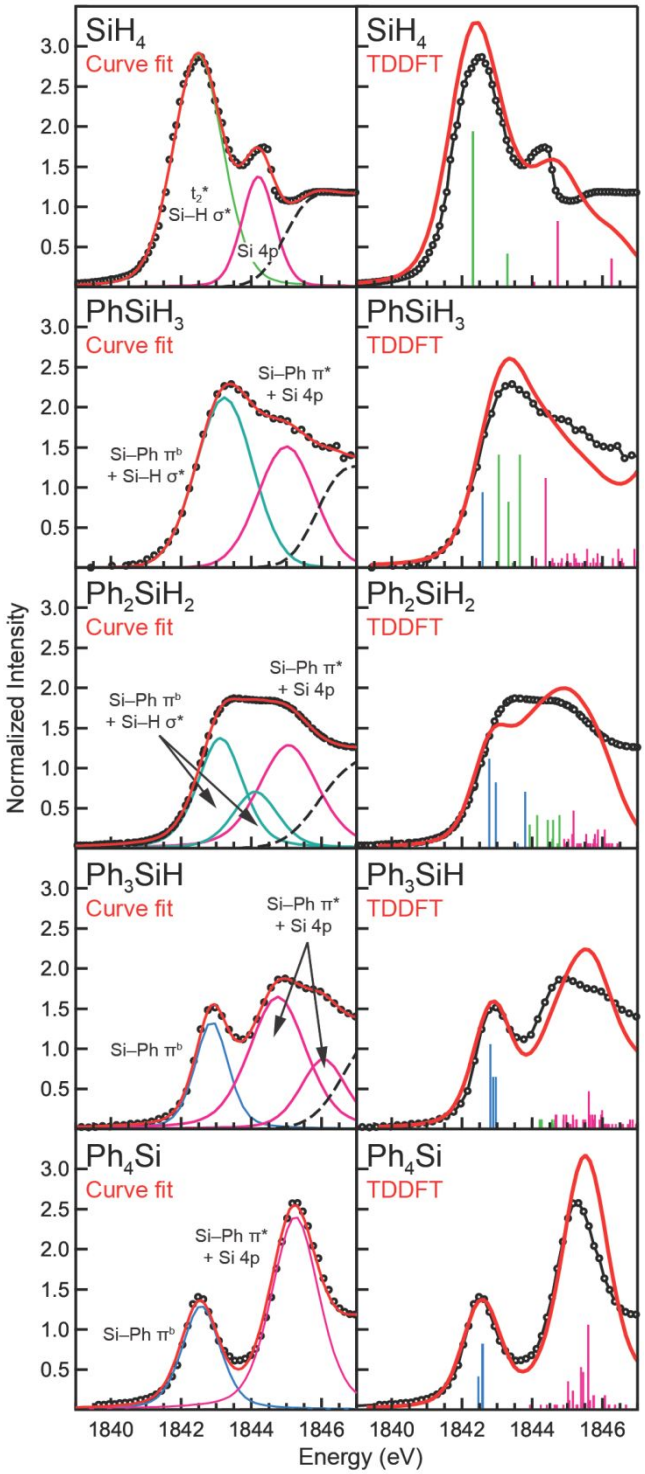

Fig. 2. Si K-edge XAS (black circles) for the aryl silanes Ph_nSiH_{4-n} (n = 0-4). Left: Total curve fits (red), *pseudo*-Voigt functions (green, teal, blue, and pink) and step functions (dashed black). Right: TDDFT calculated Si K-edge spectra (red) and individual transitions (vertical green, blue, and pink bars).

Table 1. Comparison of the experimental (XAS) and calculated (TDDFT) Si K-edge pre-edge peak energies (eV), intensities (Int) and TDDFT oscillator strengths (*f*; summed over each peak and normalized to the first transition of Ph_4Si).

	Energy (eV)[a]		Intensity (Int)[b]	
Final State Orbital	XAS	TDDFT	XAS	TDDFT
	SiH_4[24]			
1s → Si-H σ* (t_2)	1842.5	1842.5	5.6(8)	7.06
1s → Si 4p	1844.2	1844.7	1.8(3)	2.65
	$PhSiH_3$			
1s → Si-Ph π^b	1843.2	1842.6	4.3(7)	0.9
1s → S-H/C σ*		1843.4		3.9
1s → Si-Ph π* + Si 4p	1845.0	1845.0	3.1(5)	3.4
	Ph_2SiH_2			
1s → Si-Ph π^b	1843.5[c]	1843.1	3.9(6)[c]	2.7
1s → S-H/C σ*		1844.4		2.0
1s → Si-Ph π* + Si 4p[c]	1845.1	1845.5	3.2(5)	2.6
	Ph_3SiH			
1s → Si-Ph π^b	1842.9	1842.9	1.8(3)	2.4
1s → S-H/C σ*	1845.1[c]	1844.3	5.5(8)[c]	0.8
1s → Si-Ph π* + Si 4p[c]		1845.5		4.2
	Ph_4Si			
1s → Si-Ph π^b	1842.6	1842.6	2.1(3)	2.1
1s → Si-Ph π* + Si 4p	1845.3	1845.3	4.8(7)	3.9

[a] TDDFT energies are shifted by *ca.* 4 eV (see Experimental Details). [b] XAS intensities are determined from the area under the *pseudo*-Voigt functions and have an estimated error of 15%. TDDFT intensities are taken from the oscillator strengths and scaled to facilitate direct comparison with the experimental data (*ca.* 500 for each compound, based on the first Ph_4Si transition). [c] The experimental XAS peak energies and intensities for these transitions were determined by calculating the weighted average and sum, respectively, of the two functions used in the fit.

The TDDFT calculations shown in Fig. 2 and Table 1 (SRC-1/6-311(2+,2+)G**) are consistent with the STXM-XAS data and with the previously reported gas-phase spectrum for SiH_4 which exhibits one intense feature at 1842.5 eV (Si 1s → t_2).[22] The Si 1s → a_1 transition for SiH_4 is dipole forbidden ($^1A_1 \rightarrow {}^1A_1$) and not observed. Features observed at higher energies (e.g., at 1844.7 eV) are attributed to transitions involving Si 4p orbitals, and not reflective of ground-state orbital mixing.[30,33-35] The electronic structures of the aryl silanes are quite different from SiH_4 because the Si 3p orbitals can participate in both Si-C σ-bonds and Si-Ph π-bonds involving the aromatic rings. To facilitate interpretation of the Si K-edge results, it is instructive to differentiate the valence molecular orbitals (MOs) in $PhSiH_3$ from those in SiH_4. As shown in Fig. 3, substitution of a hydride in SiH_4 for a Ph reduces the symmetry from T_d to pseudo-C_s, such that the previously degenerate 3p orbitals take on a′ + a′ + a″ symmetries (p_x, p_y, and p_z, respectively). The 3s, $3p_x$, and $3p_z$ atomic orbitals (AOs) in $PhSiH_3$ largely comprise a band of Si-H and Si-C σ* MOs that have 1a″ + 3a′ + 2a″ symmetry (Fig. 3, green). The Si $3p_y$ AO is unique because it is parallel to the six C 2p orbitals making up the π-system of the aryl groups. Mixing between the Si $3p_y$ and phenyl ring results in formation of new Si-Ph π^b (1a′ and 2a′, blue) and Si-Ph π* (4a′ and 5a′, pink) MOs. These new π^b and π* MOs are stabilized and destabilized, respectively relative to the Si-H and Si-C σ* MOs. Fig. 3 shows that the Si-Ph π^b and π* MOs of $PhSiH_3$ can also engage in some symmetry allowed Si-H σ* mixing.

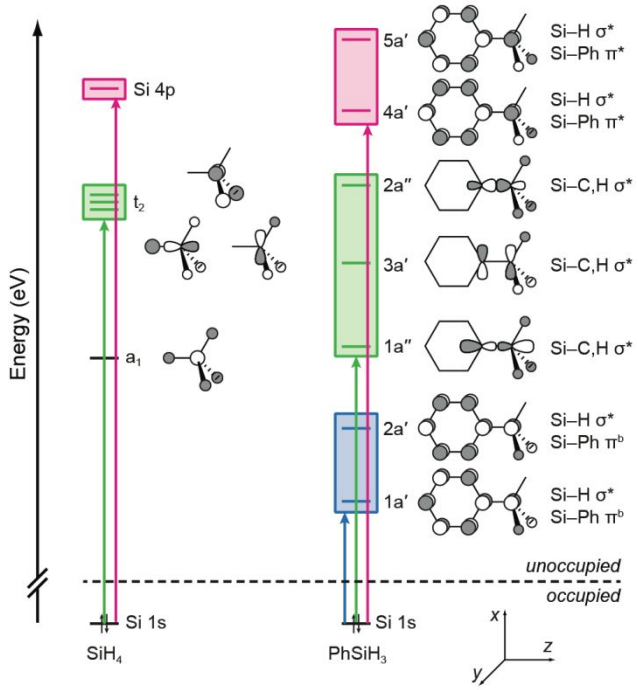

Fig. 3. Qualitative molecular orbital correlation diagram showing formation of $PhSiH_3$ valence orbitals in idealized C_s symmetry from T_d-SiH_4, and representations of the nodal characteristics in the bonding and antibonding interactions.

Inspection of the natural transition orbitals (NTOs) provided by the TDDFT calculations for $PhSiH_3$ shows consistency with the group theory predictions (Fig. 4). For example, the TDDFT shows transitions centered at 1843.5 eV involving purely Si-H and Si-C σ* orbitals derived from the Si $3p_x$ and $3p_z$ orbitals (Si 1s → 1a″ + 3a′ + 2a″), which are related to the Si 1s → t_2 transition for SiH_4. The TDDFT also shows new transitions at lower energy (1842.6 eV) that involve $3p_y$-derived orbitals with Si-Ph π^b and Si-H σ* character (Si 1s → 1a′ + 2a′). In the experimental spectrum, a single function centered at 1843.2 eV is used to model these low energy transitions involving the Si-Ph π^b orbitals and Si-H/C σ* orbitals. Moving to higher energy, the second function at 1845.0 eV is attributed to multiple transitions involving the Si-Ph π* orbitals (Si 1s → 4a′ + 5a′). The TDDFT calculations indicate that these Si 1s → 4a′ + 5a′ transitions are at similar energies as additional transitions into the high energy Si 4p orbitals that are not deconvoluted in the curve fit of the experimental data.

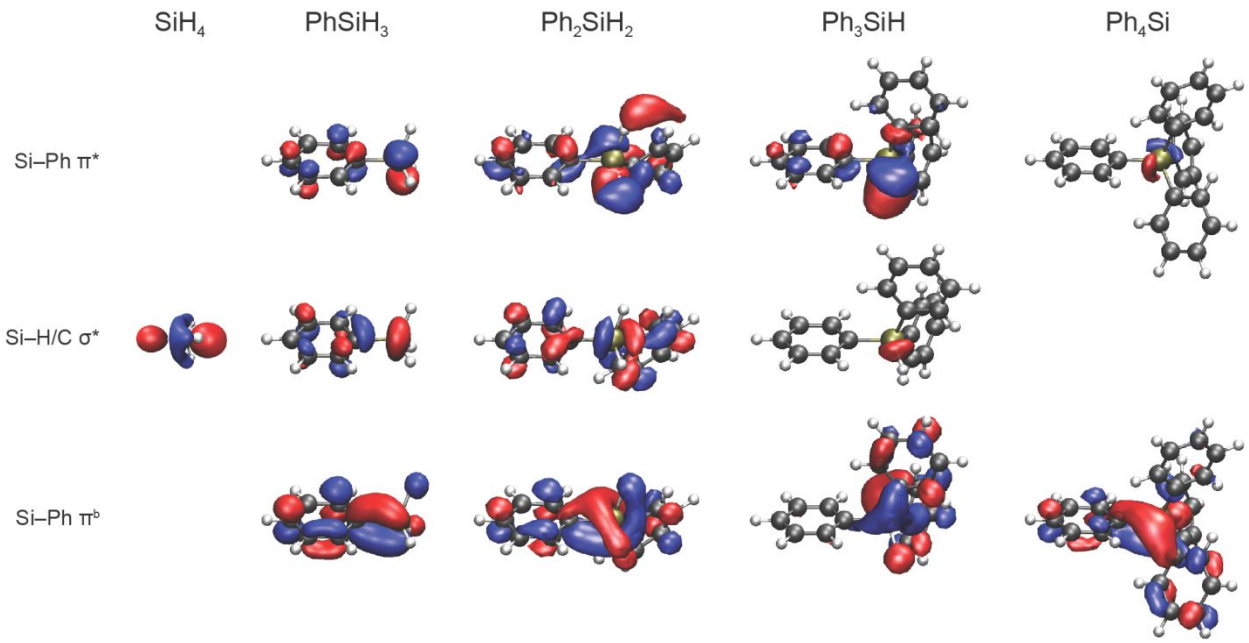

Fig. 4. TDDFT-calculated NTOs for selected Si K-edge XAS transitions.

The TDDFT calculations and isosurface plots support an analogous interpretation for Ph_2SiH_2 and Ph_3SiH in which the low energy functions are assigned to transitions to predominantly Si-Ph π^b orbitals and intermediate-energy functions to transitions into Si-H and Si-C σ* orbitals. For Ph_3SiH, the Si-H and Si-C σ* orbitals were predicted to be weak and nearly indistinguishable from the baseline. Hence, the two functions that were required to model the high energy regions for Ph_3SiH were both attributed primarily to transitions from the Si 1s to predominantly Si-Ph π* orbitals and Si 4p orbitals. For Ph_4Si, which has higher symmetry that can be approximated as T_d, the two features are assigned to Si 1s → t_2 (Si-Ph π^b) and Si 1s → t_2* (Si-Ph π*) transitions. Support for these assignments is provided by a P K-edge XAS study from Daly and coworkers, which provided a t_2–t_2* splitting of 2.9 eV for the isoelectronic Ph_4P^{1+} cation that is similar to values found for Ph_4Si using XAS (2.7 eV) and TDDFT (2.8 eV).[36]

Fig. 5 compares the experimental XAS and TDDFT calculated splittings as a function of aryl substitution. Differences in splitting between groups of transitions observed at low energy and those at higher energy measured with XAS were not significant when the silanes differed by one aryl substituent, after accounting for uncertainty in the curve fit models and sources of experimental error. A significant trend towards increased splitting was observed in the XAS data for the complete series, from 1.7(2) eV for SiH_4 and 1.8(2) eV for $PhSiH_3$, to 2.7(2) eV for Ph_4Si. An upwards trend in the TDDFT data was also observed, from 2.2 eV for SiH_4 and 2.5 eV for $PhSiH_3$, to 2.8 eV for Ph_4Si. Comparing the XAS and TDDFT data, we see that the experimental trend is exaggerated because the Si 1s → π^b transitions are convolved with higher energy Si 1s → Si-H/C σ* transitions in the curve fit of the experimental data and individually resolved with

TDDFT calculations. As the number of aryl substituents increases for Ph_3SiH and Ph_4Si and the amplitudes of the Si 1s → Si-H/C σ* transitions decrease, the quantitative agreement between XAS and TDDFT improves. Taken together, the overall increase in splitting points to greater energetic stabilization of the π^b orbitals and destabilization of the π* orbitals with steady rise in the number of π-orbital interactions.

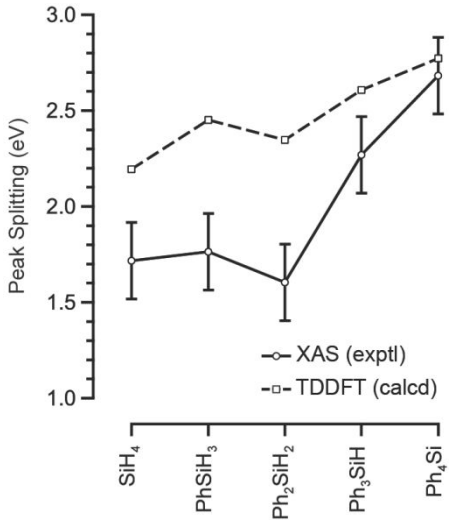

Fig. 5. Plot comparing the experimental (solid line) and calculated (dashed line) splittings between the low energy Si 1s → Si-Ph π^b transitions and high energy (1s → Si-Ph π* + Si 4p transitions). Both the XAS and TDDFT results suggest that there is an increase in splitting between the bonding and antibonding orbitals with more phenyl substituents. Discrepancies between the XAS and TDDFT results for $PhSiH_3$ and Ph_2SiH_2 can be partially attributed to convolution of the Si 1s → Si-Ph π^b and 1s → S-H/C σ* transitions, which are not resolved in the experimental data.

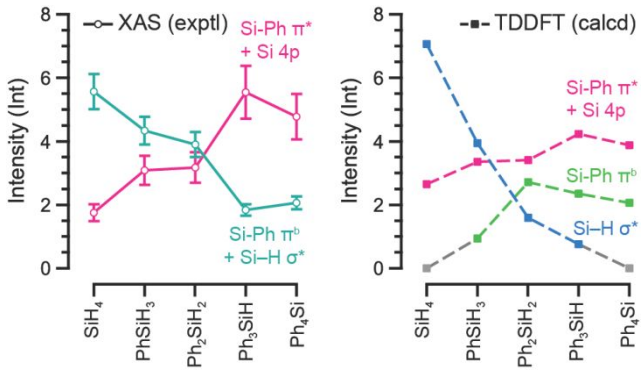

Fig. 6. Plots showing the XAS (solid) and TDDFT (dashed) Si K-edge transition intensities provided in Table 1. Both the experimental and theoretical results show a decrease in Si 3p character in the Si-H σ* orbitals and concomitant increase in Si 3p character in the π^b and π*orbitals with greater phenyl substitution.

Because the probability of a Si K-edge transition is weighted by the amount of Si 3p character in the final state MO, the XAS and TDDFT intensities provided in Table 1 and Fig. 6 can be used to evaluate relative changes in Si 3p orbital mixing. For example, the XAS shows that the low energy features steadily decrease in amplitude beginning with SiH_4 and ending with Ph_4Si, from 5.6(8) to 2.1(3), respectively. TDDFT calculations reveal more nuanced behavior, showing a dramatic drop in Si 1s → Si-H/C σ* transition intensities from 7.1 to 0.8 for SiH_4 and Ph_3SiH, while Si 1s → π^b transition intensities rise from 0.9 for $PhSiH_3$ to 2.1 for Ph_4Si. This pattern reflects a steady increase in Si-Ph π-mixing with increasing aryl substitution that is offset by a decrease in Si-H bonding. Likewise, intensities for the high energy features corresponding Si-Ph π* orbitals also increase from $PhSiH_3$ (XAS: 3.1(5), TDDFT: 3.4) to Ph_4Si (XAS: 4.9(7), TDDFT: 3.9), also reflecting more Si-Ph π-mixing with larger numbers of aryl substituents.

Taken together, the consistent trends observed in the experimental and TDDFT calculated Si K-edge XAS support an intuitive picture of valence bonding in the Ph_nSiH_{4-n} series. Introducing aryl substituents splits the Si-H σ* orbitals (t_2*) for SiH_4 and results in formation of new Si-Ph π^b and π* orbitals that are stabilized and destabilized, respectively, relative to the remaining Si-H σ* orbitals. As the number of Si-Ph π interactions increases, the greater involvement of the Si 3p orbitals in Si-Ph bonding is reflected in the Si K-edge XAS by more intense transitions to both the Si-Ph π^b and π* valence orbitals and weaker transitions to the Si-H σ* orbitals.

The reactivity of aryl silanes is driven in part by the composition of the LUMOs and the accessibility of pathways for electron delocalization through conjugation with aryl groups. This conclusion is consistent with earlier DFT calculations,[37] which showed that hydride donor abilities increase (i.e. a decreased ΔG for hydride dissociation from the silyl cation) with increasing aryl substitution from SiH_4 (116.67 kcal/mol) to $PhSiH_3$ (104.62 kcal/mol) to Ph_2SiH_2 (98.31 kcal/mol) to Ph_3SiH (93.19 kcal/mol). Likewise, thermochemical investigations of organosilicon compounds have shown that the homolytic Si-H bond dissociation energies decrease by a very small amount with increasing phenyl substitution from SiH_4 (91.7 kcal/mol) to $PhSiH_3$ (91.2 kcal/mol) to Ph_2SiH_2 (90.5 kcal/mol) and Ph_3SiH (88.6 kcal/mol).[38] The Si K-edge XAS and TDDFT results described above show that, beginning with SiH_4, each successive addition of an aryl substituent lessens the amount of Si-H orbital mixing as the Si 3p orbitals become increasingly dominated by π-interactions with the Ph groups. In alternative terminology, the more aryl-substituted silanes are primed for hydride donation by formation of resonance-stabilized silyl cations, which are often invoked during theoretical rationales for silane rearrangements and catalytic mechanisms.[7,13] The Si K-edge XAS results provided herein constitute new experimental evidence for this effect by investigation of the valence electronic structure.

These results show that Si K-edge XAS can discern changes in Si character that occur in specific σ- or π-bonding orbitals, which will compliment measurements of the total bonding interaction given by bond

lengths, bond strengths, and ^{29}Si NMR chemical shifts. Developing accurate models of the experimental spectra is best achieved with the aid of calculations, and by examining trends systematically in a series of analogous compounds. Recent innovations in synchrotron instrumentation including high resolution spectrometers for the tender X-ray energy regime (~1500 to 5000 eV) will enable future measurements at the Si K-edge.[39-42] Building on these initial Si K-edge results for liquid samples, future work will monitor the chemical structure of hydrosilation catalysts, intermediates, and substrates through dynamic, in situ Si K-edge XAS experiments.

EXPERIMENTAL DETAILS

STXM Sample Preparation

All manipulations were performed with rigorous exclusion of air and moisture using Schlenk and glovebox techniques under an argon atmosphere. Samples of Ph_4Si, Ph_3SiH, Ph_2SiH_2 and $PhSiH_3$ were obtained from Aldrich and dried under vacuum or using 4Å molecular sieves prior to use. For solid samples of Ph_4Si or Ph_3SiH, a small amount of pulverized crystalline analyte was applied to a Si_3N_4 window (100 nm, Silson) using a fiber brush. A second window was placed over the sample, essentially sandwiching the crystals, and the windows were sealed together using Hardman Double/Bubble epoxy. Liquid samples were prepared using a commercially-available microfluidic cell (Silson) consisting of two 50 nm Si_3N_4 membranes separated by a 10 μm thick SU–8 gasket. A droplet of Ph_2SiH_2 or $PhSiH_3$ was applied to the Si_3N_4 window fitted with the gasket. The second window was placed on top while allowing excess liquid to flow from the edges of the sample, and the windows were held together with a 3D-printed plastic clip (Silson).

Silicon K-Edge STXM Measurements

STXM methodology was similar to that discussed previously.[31,43] Single-energy images and silicon K-edge XAS spectra were acquired using the STXM instruments at the at the Canadian Light Source (CLS) spectromicroscopy beamline 10ID-1 and at the Advanced Light Source-Molecular Environmental Science (ALS-MES) beamline 11.0.2. The CLS operated in decay mode (250 to 150 mA) while the ALS operated in topoff mode (500 mA). At both facilities, the beamlines operated with a 0.5 atm He-filled chamber and used elliptically polarizing undulators that delivered photons to entrance slit-less plane-grating monochromators.[44-46] This provides a 130 to 2700 eV working energy range at the CLS, and a 90 to 1950 eV working energy range at the ALS. Energy calibrations were performed at the Si K-edge for Si (1839.2 eV).[24] The energy resolution $E/\Delta E$ was estimated at 5,000 for both beamlines,[44-45] which is consistent with the observed standard deviation for spectral transitions of ± 0.3 eV determined from comparison of spectral features over multiple samples and beam runs.

For all measurements, the X-ray beam was focused with a zone plate (35 nm) onto the sample, and the transmitted light was detected. Images at a single energy were obtained by raster-scanning the sample and collecting transmitted monochromatic light as a function of sample position. For solid samples, spectra at each image pixel or particular regions of interest on the sample image were extracted from the "stack", which is a collection of images recorded at multiple, closely spaced photon energies across the absorption edge. Dwell times used to acquire an image at a single photon energy were typically 2 ms per pixel. To quantify the absorbance signal, the measured transmitted intensity (I) was converted to optical density using Beer−Lambert's law: $OD = \ln(I/I_0) = \mu\rho d$, where I_0 is the incident photon flux intensity, d is the sample thickness, and μ and ρ are the mass absorption coefficient and density of the sample material, respectively. Incident beam intensity was measured through the sample-free region of the Si_3N_4 windows. Spectra were then obtained by averaging over the crystallites deposited on the substrate. Regions of particles with an absorption of >1.5 OD were omitted to ensure the spectra were in the linear regime of the Beer−Lambert law. For liquid samples, the transmitted intensity (I) was measured with a defocused beam (~20 μm spot size) at a single position on the solution cell. Incident photon flux (I_0) was measured immediately prior to or after the sample scan through a blank Si_3N_4 window (100 nm, Silson) mounted at a different position on the same sample holder. Dwell times were 2000 ms per photon energy. During the STXM experiments, samples showed no sign of radiation damage, and each spectrum was reproduced from multiple independent samples.

Data Analysis

The data were normalized in MATLAB using the MBACK algorithm, and by setting the edge jump at 1839 eV to an intensity of 1.0.[47] Fits to the Si K-edges were performed using the program IGOR 6.37 and a modified version of EDG_FIT.[48] Second derivative spectra were used as guides to determine the number and position of fit functions, and the number of parameters associated with the fit functions was minimized to avoid exceeding the resolution limit. Rising edge features were modeled using Gaussian functions and an error function. Pre-edge features were modelled by pseudo-Voigt line shapes with a variable ratio (η) of Gaussian and Lorentzian contributions. The area under the pre-edge peaks (defined as the intensity) was calculated with the formula $ph \times hwhm \times \{ \eta [\pi / ln(2)]^{1/2} + (1- \eta) \pi \}$, where ph = peak height (normalized intensity), fwhm = full-width at half maximum height (eV). Pre-edge intensities are reported with a standard deviation of 15% based on data reproducibility. To minimize the number of parameters, a constraint was applied requiring that the value of η be between 0.65 and 0.70 for each pseudo-Voigt function. This range was established based on the combined effect of broadening from instrumental limitations ($\sigma \approx 0.7$ eV)[44-45] and Si 1s core-hole lifetimes (~ 0.4 eV FWHM).[49] For $PhSiH_3$, functions with pure Gaussian character were used to account for the presence of a large number of evenly-spaced transitions. For SiH_4 a value of η =

0.83 was obtained after an unconstrained fit, which reflects increased instrumental broadening for the Si K-edge measurement of SiH_4.[22] The validity of each curve fit was determined by good correlation coefficients, residual intensities (data minus fit) that should resemble horizontal lines at zero, and symmetric residual peaks that should be similar in shape to the corresponding pseudo-Voigt functions. For $PhSiH_3$ and Ph_2SiH_2, fully unconstrained models resulted in unrealistically broad features (FWHM > 2 eV); in these cases, an additional constraint was applied requiring that the two lowest energy functions used to model the pre-edge region had equal widths (FWHM).

Electronic Structure Calculations

Density functional theory calculations were performed using Q Chem 5.0.0[50] on the Tiger cluster at UC Berkeley Molecular Graphics and Computing Facility. The gas-phase structures of the the H_nSiPh_{4-n} compounds were optimized at the B3LYP/6-311G** level of theory prior to their use in time-dependent density functional theory (TDDFT) calculations.

Simulated Si K-Edge Spectra

For the H_nSiPh_{4-n} compounds, the Si K-edge XAS were simulated (TDDFT). For these computations, the short-range corrected (SRC) functional of Besley and coworkers was used with the 6-311G** basis set.[32] This functional has been specifically parametrized to perform well for TDDFT simulations of XAS, by including a greater degree of exact exchange at short range. This TDDFT analysis involves a linear response calculation generating the transition densities and transition dipoles between the calculated excited states and the ground states.[51-53] The excitations originating from all of the intermediate states between the Si 1s and the HOMO were excluded so that only excitations from the core levels to virtual molecular orbitals could be analyzed. This allows the virtual orbitals to mix and reflect the presence of the silicon core hole. Relaxations for the other occupied orbitals associated with the core hole are not included. Shifts applied are 3.18, 4.27, 4.64, 4.42, and 4.13 eV for SiH_4, $PhSiH_3$, Ph_2SiH_2, Ph_3SiH, and Ph_4Si, respectively.[19,30,35] These shifts are comparable to those attributed to relativistic corrections by Besley and coworkers in the development of the SRC functional. Simulated spectra for $PhSiH_3$, Ph_2SiH_2, Ph_3SiH, and Ph_4Si were obtained by broadening with a Voigt function with half-widths at half-maximum of 0.21 eV and 0.52 eV for the Lorentzian and Gaussian components, respectively, to account for the core-hole and instrumental broadening (see above). The simulated spectrum for SiH_4 was obtained with an increased Gaussian width of 0.71 eV (HWHM) to account for differences in the reported energy resolution (σ = 0.5 eV).[22]

AUTHOR CONTRIBUTIONS

Minasian and Phillips performed the XAS experiments and Smith performed the DFT calculations. All

authors interpreted the data and wrote the manuscript.

CONFLICTS OF INTEREST

There are no conflicts to declare.

ACKNOWLEDGMENTS

This work was supported by Laboratory Directed Research and Development (LDRD) funding from Berkeley Lab, provided by the Director, Office of Science of the U.S. Department of Energy under Contract No. DE-AC02-05CH1123. PWS was supported by the National Science Foundation under grant CHE-1566538. Research at Beamline 11.0.2 at the ALS was supported at LBNL by the Director, Office of Science, Office of Basic Energy Sciences, Division of Chemical Sciences, Geosciences, and Biosciences Condensed Phase and Interfacial Molecular Sciences Program of the U.S. DOE under Contract DEAC02-05CH11231. Research described in this paper was also conducted at the Canadian Light Source, which is supported by the Canada Foundation for Innovation, Natural Sciences and Engineering Research Council of Canada, the University of Saskatchewan, the Government of Saskatchewan, Western Economic Diversification Canada, the National Research Council Canada, and the Canadian Institutes of Health Research. Computations were performed at the UC Berkeley Molecular Graphics and Computation Facility, which is directed by Kathleen Durkin and supported by NIH grant NIH S10OD023532.

REFERENCES

1. B. Marciniec, *Hydrosilylation: A Comprehensive Review on Recent Advances*, Springer, The Netherlands, 2009.
2. B. Marciniec, *Comprehensive Handbook on Hydrosilylation*, Pergamon Press, Tarrytown, NY, 1992.
3. B. Marciniec, *Appl. Organomet. Chem.*, 2000, **14**, 527-538.
4. M. Oestreich, J. Hermeke and J. Mohr, *Chem. Soc. Rev.*, 2015, **44**, 2202-2220.
5. A. J. Chalk and J. F. Harrod, *J. Am. Chem. Soc.*, 1965, **87**, 16-21.
6. Y. Nakajima and S. Shimada, *RSC Adv.*, 2015, **5**, 20603-20616.
7. M. C. Lipke, A. L. Liberman-Martin and T. D. Tilley, *Angew. Chem. Int. Ed.*, 2017, **56**, 2260-2294.
8. A. Y. Houghton, J. Hurmalainen, A. Mansikkamaki, W. E. Piers and H. M. Tuononen, *Nat. Chem.*, 2014, **6**, 983-988.
9. D. J. Parks and W. E. Piers, *J. Am. Chem. Soc.*, 1996, **118**, 9440-9441.
10. D. L. Lichtenberger and A. Raichaudhuri, *J. Am. Chem. Soc.*, 1991, **113**, 2923-2930.
11. M. Rauch and G. Parkin, *J. Am. Chem. Soc.*, 2017, **139**, 18162-18165.
12. Q. H. Zhou and Y. X. Li, *J. Am. Chem. Soc.*, 2015, **137**, 10182-10189.
13. A. Schafer, M. Reissmann, A. Schafer, W. Saak, D. Haase and T. Muller, *Angew. Chem. Int. Ed.*, 2011, **50**, 12636-12638.
14. A. Chantzis, J. K. Kowalska, D. Maganas, S. DeBeer and F. Neese, *J. Chem. Theory Comput.*, 2018, **14**, 3686-3702.
15. F. M. F. de Groot, *Inorg. Chim. Acta*, 2008, **361**, 850-856.

16. J. T. Lukens, I. M. DiMucci, T. Kurogi, D. J. Mindiola and K. M. Lancaster, *Chem. Sci.*, 2019, **10**, 5044-5055.
17. S. D. George, K. W. Huang, R. M. Waymouth and E. I. Solomon, *Inorg. Chem.*, 2006, **45**, 4468-4477.
18. S. R. Daly, J. M. Keith, E. R. Batista, K. S. Boland, D. L. Clark, S. A. Kozimor and R. L. Martin, *J. Am. Chem. Soc.*, 2012, **134**, 14408-14422.
19. S. G. Minasian, J. M. Keith, E. R. Batista, K. S. Boland, J. A. Bradley, S. R. Daly, D. Sokaras, S. A. Kozimor, W. W. Lukens, R. L. Martin, D. Nordlund, G. T. Seidler, D. K. Shuh, T. Tyliszczak, G. L. Wagner, T. C. Weng and P. Yang, *J. Am. Chem. Soc.*, 2013, **135**, 1864-1871.
20. C. M. Donahue, S. P. McCollom, C. M. Forrest, A. V. Blake, B. J. Bellott, J. M. Keith and S. R. Daly, *Inorg. Chem.*, 2015, **54**, 5646-5659.
21. S. Bodeur, P. Millie, E. L. Alugrin, I. Nenner, A. Filipponi, F. Boscherini and S. Mobilio, *Phys. Rev. A*, 1989, **39**, 5075-5081.
22. S. Bodeur, P. Millie and I. Nenner, *Phys. Rev. A*, 1990, **41**, 252-263.
23. D. G. J. Sutherland, M. Kasrai, G. M. Bancroft, Z. F. Liu and K. H. Tan, *Phys. Rev. B*, 1993, **48**, 14989-15001.
24. S. G. Urquhart, J. Z. Xiong, A. T. Wen, T. K. Sham, K. M. Baines, G. G. B. Desouza and A. P. Hitchcock, *Chem. Phys.*, 1994, **189**, 757-768.
25. P. Ildefonse, G. Calas, A. M. Flank and P. Lagarde, *Nucl. Instrum. Methods Phys. Res. Sect. B-Beam Interact. Mater. Atoms*, 1995, **97**, 172-175.
26. J. Z. Xiong, D. T. Jiang, Z. F. Liu, K. M. Baines, T. K. Sham, S. G. Urquhart, A. T. Wen, T. Tyliszczak and A. P. Hitchcock, *Chem. Phys.*, 1996, **203**, 81-92.
27. S. G. Urquhart, C. C. Turci, T. Tyliszczak, M. A. Brook and A. P. Hitchcock, *Organometallics*, 1997, **16**, 2080-2088.
28. S. G. Urquhart, A. P. Hitchcock, J. F. Lehmann and M. Denk, *Organometallics*, 1998, **17**, 2352-2360.
29. J. Z. Xiong, D. T. Jiang, C. E. Dixon, K. M. Baines and T. K. Sham, *Can. J. Chem.*, 1996, **74**, 2229-2239.
30. S. G. Minasian, J. M. Keith, E. R. Batista, K. S. Boland, S. A. Kozimor, R. L. Martin, D. K. Shuh, T. Tyliszczak and L. J. Vernon, *J. Am. Chem. Soc.*, 2013, **135**, 14731-14740.
31. A. B. Altman, C. D. Pemmaraju, C. Camp, J. Arnold, S. G. Minasian, D. Prendergast, D. K. Shuh and T. Tyliszczak, *J. Am. Chem. Soc.*, 2015, **137**, 10304-10316.
32. N. A. Besley, M. J. G. Peach and D. J. Tozer, *Phys. Chem. Chem. Phys.*, 2009, **11**, 10350-10358.
33. A. T. Wen and A. P. Hitchcock, *Can. J. Chem.*, 1993, **71**, 1632-1644.
34. M. Casarin, P. Finetti, A. Vittadini, F. Wang and T. Ziegler, *J. Phys. Chem. A*, 2007, **111**, 5270-5279.
35. S. G. Minasian, J. M. Kieth, E. R. Batista, K. S. Boland, C. N. Christensen, D. L. Clark, S. D. Conradson, S. A. Kozimor, R. L. Martin, D. E. Schwarz, D. K. Shuh, G. L. Wagner, M. P. Wilkerson, L. E. Wolfsberg and P. Yang, *J. Am. Chem. Soc.*, 2012, **134**, 5586-5597.
36. A. V. Blake, H. C. Wei, C. M. Donahue, K. Lee, J. M. Keith and S. R. Daly, *J. Synchrotron Rad.*, 2018, **25**, 529-536.
37. Z. M. Heiden and A. P. Lathem, *Organometallics*, 2015, **34**, 1818-1827.
38. R. Becerra and R. Walsh, in *The Chemistry of Organosilicon Compounds*, eds. Z. Rappaport and Y. Apeloig, Wiley, Chichester, 1998, vol. 2, pp. 153-180.
39. B. Abraham, S. Nowak, C. Weninger, R. Armenta, J. Defever, D. Day, G. Carini, K. Nakahara, A. Gallo, S. Nelson, D. Nordlund, T. Kroll, M. S. Hunter, T. van Driel, D. L. Zhu, T. C. Weng, R. Alonso-Mori and D. Sokaras, *J. Synchrotron Rad.*, 2019, **26**, 629-634.
40. P. Northrup, *J. Synchrotron Rad.*, 2019, **26**, 2064-2074.
41. S. H. Nowak, R. Armenta, C. P. Schwartz, A. Gallo, B. Abraham, A. T. Garcia-Esparza, E. Biasin, A. Prado, A. Maciel, D. Zhang, D. Day, S. Christensen, T. Kroll, R. Alonso-Mori, D. Nordlund, T. C. Weng and D. Sokaras, *Rev. Sci. Instrum.*, 2020, **91**.

42. M. Rovezzi, A. Harris, B. Detlefs, T. Bohdan, A. Svyazhin, A. Santambrogio, D. Degler, R. Baran, B. Reynier, P. N. Crespo, C. Heyman, H. P. Van Der Kleij, P. Van Vaerenbergh, P. Marion, H. Vitoux, C. Lapras, R. Verbeni, M. M. Kocsis, A. Manceau and P. Glatzel, *J. Synchrotron Rad.*, 2020, **27**, 813-826.
43. A. B. Altman, C. D. Pemmaraju, S. Alayoglu, J. Arnold, C. H. Booth, A. Braun, C. E. Bunker, A. Herve, S. G. Minasian, D. Prendergast, D. K. Shuh and T. Tyliszczak, *Inorg. Chem.*, 2017, **56**, 5710-5719.
44. K. V. Kaznatcheev, C. Karunakaran, U. D. Lanke, S. G. Urquhart, M. Obst and A. P. Hitchcock, *Nucl. Instrum. Methods Phys. Res. A*, 2007, **582**, 96-99.
45. H. Bluhm, K. Andersson, T. Araki, K. Benzerara, G. E. Brown, J. J. Dynes, S. Ghosal, M. K. Gilles, H. C. Hansen, J. C. Hemminger, A. P. Hitchcock, G. Ketteler, A. L. D. Kilcoyne, E. Kneedler, J. R. Lawrence, G. G. Leppard, J. Majzlan, B. S. Mun, S. C. B. Myneni, A. Nilsson, H. Ogasawara, D. F. Ogletree, K. Pecher, M. Salmeron, D. K. Shuh, B. Tonner, T. Tyliszczak, T. Warwick and T. H. Yoon, *J. Electron. Spectrosc. Relat. Phenom.*, 2006, **150**, 86-104.
46. H. J. Nilsson, T. Tyliszczak, R. E. Wilson, L. Werme and D. K. Shuh, *Anal. Bioanal. Chem.*, 2005, **383**, 41-47.
47. T. C. Weng, G. S. Waldo and J. E. Penner-Hahn, *J. Synchrotron Rad.*, 2005, **12**, 506-510.
48. G. N. George, Stanford Synchrotron Radiation Laboratory, Stanford Linear Accelerator Center, Stanford Synchrotron Radiation Laboratory, Stanford Linear Accelerator Center: Stanford, CA.
49. O. Keski-Rahkonen and M. O. Krause, *At. Data Nucl. Data Tables*, 1974, **14**, 139-146.
50. Y. H. Shao, Z. T. Gan, E. Epifanovsky, A. T. B. Gilbert, M. Wormit, J. Kussmann, A. W. Lange, A. Behn, J. Deng, X. T. Feng, D. Ghosh, M. Goldey, P. R. Horn, L. D. Jacobson, I. Kaliman, R. Z. Khaliullin, T. Kus, A. Landau, J. Liu, E. I. Proynov, Y. M. Rhee, R. M. Richard, M. A. Rohrdanz, R. P. Steele, E. J. Sundstrom, H. L. Woodcock, P. M. Zimmerman, D. Zuev, B. Albrecht, E. Alguire, B. Austin, G. J. O. Beran, Y. A. Bernard, E. Berquist, K. Brandhorst, K. B. Bravaya, S. T. Brown, D. Casanova, C. M. Chang, Y. Q. Chen, S. H. Chien, K. D. Closser, D. L. Crittenden, M. Diedenhofen, R. A. DiStasio, H. Do, A. D. Dutoi, R. G. Edgar, S. Fatehi, L. Fusti-Molnar, A. Ghysels, A. Golubeva-Zadorozhnaya, J. Gomes, M. W. D. Hanson-Heine, P. H. P. Harbach, A. W. Hauser, E. G. Hohenstein, Z. C. Holden, T. C. Jagau, H. J. Ji, B. Kaduk, K. Khistyaev, J. Kim, J. Kim, R. A. King, P. Klunzinger, D. Kosenkov, T. Kowalczyk, C. M. Krauter, K. U. Lao, A. D. Laurent, K. V. Lawler, S. V. Levchenko, C. Y. Lin, F. Liu, E. Livshits, R. C. Lochan, A. Luenser, P. Manohar, S. F. Manzer, S. P. Mao, N. Mardirossian, A. V. Marenich, S. A. Maurer, N. J. Mayhall, E. Neuscamman, C. M. Oana, R. Olivares-Amaya, D. P. O'Neill, J. A. Parkhill, T. M. Perrine, R. Peverati, A. Prociuk, D. R. Rehn, E. Rosta, N. J. Russ, S. M. Sharada, S. Sharma, D. W. Small, A. Sodt, T. Stein, D. Stuck, Y. C. Su, A. J. W. Thom, T. Tsuchimochi, V. Vanovschi, L. Vogt, O. Vydrov, T. Wang, M. A. Watson, J. Wenzel, A. White, C. F. Williams, J. Yang, S. Yeganeh, S. R. Yost, Z. Q. You, I. Y. Zhang, X. Zhang, Y. Zhao, B. R. Brooks, G. K. L. Chan, D. M. Chipman, C. J. Cramer, W. A. Goddard, M. S. Gordon, W. J. Hehre, A. Klamt, H. F. Schaefer, M. W. Schmidt, C. D. Sherrill, D. G. Truhlar, A. Warshel, X. Xu, A. Aspuru-Guzik, R. Baer, A. T. Bell, N. A. Besley, J. D. Chai, A. Dreuw, B. D. Dunietz, T. R. Furlani, S. R. Gwaltney, C. P. Hsu, Y. S. Jung, J. Kong, D. S. Lambrecht, W. Z. Liang, C. Ochsenfeld, V. A. Rassolov, L. V. Slipchenko, J. E. Subotnik, T. Van Voorhis, J. M. Herbert, A. I. Krylov, P. M. W. Gill and M. Head-Gordon, *Mol. Phys.*, 2015, **113**, 184-215.
51. S. Hirata and M. Head-Gordon, *Chem. Phys. Lett.*, 1999, **314**, 291-299.
52. S. Hirata and M. Head-Gordon, *Chem. Phys. Lett.*, 1999, **302**, 375-382.
53. E. Runge and E. K. U. Gross, *Phys. Rev. Lett.*, 1984, **52**, 997-1000.